Projected Changes of Kuroshio in a Warming Climate

JO-HSU HUANG,[a] YU-HENG TSENG,[a,b] AND YI-CHUN KUO[a]
[a] *Institute of Oceanography, National Taiwan University, Taipei, Taiwan*
[b] *Ocean Center, National Taiwan University, Taipei, Taiwan*

(Manuscript received 10 February 2024, in final form 15 August 2024, accepted 4 September 2024)

ABSTRACT: The projected changes in the Kuroshio and the associated mechanisms in response to future warming scenarios remain unclear. While some studies propose a negative midlatitude wind stress curl (WSC) tendency could expedite Kuroshio recirculation, others suggest that the isopycnal transport of warmer subtropical mode water (STMW) to the east of the Kuroshio enhances only the velocity in the upper ocean. In the future projections under the shared socioeconomic pathways 5-8.5 (SSP5-8.5) within phase 6 of Coupled Model Intercomparison Project (CMIP6) model ensemble, a consistent enhancement of the Kuroshio along the Japanese coast (JP-Kuroshio) is observed. Particularly, the response of the JP-Kuroshio to WSC changes is more pronounced in high-resolution (HR) models than low-resolution (LR) ones. However, diverse results emerge in the East China Sea (ECS-Kuroshio). While most CMIP6 HR models indicate a reduction of Kuroshio within the upper 1000 m in the ECS-Kuroshio, the ensemble of CMIP6 LR models shows an intensification of Kuroshio within the upper 300 m and a deceleration below, suggesting a consistent baroclinic feature in ECS-Kuroshio. Additional ocean model sensitivity experiments confirm that the WSC influences the Kuroshio throughout the entire water column, particularly below 300 m. Within the upper 300 m, the primary driver of Kuroshio changes is the surface warming, aligning with the STMW mechanism. Moreover, the surface salinity flux may also play an important role in the dynamics of Kuroshio changes.

KEYWORDS: Boundary currents; Eddies; Climate change; Climate prediction; Climate sensitivity; Climate variability

1. Introduction

Kuroshio, the wind-driven western boundary current (WBC) in the North Pacific, flows northward from the North Equatorial Current along the east coast of Taiwan. It separates eastward from Japan around 35°N and forms the Kuroshio Extension (KET), where strong mesoscale eddy activities exist (Tseng et al. 2012). The southern recirculation gyre (SRG), known as the Kuroshio recirculation, located to the south of the KET between 31° and 35°N, can be enhanced by potential vorticity (PV) advection or eddy dynamics, as indicated in previous studies (e.g., Marshall and Nurser 1986; Jayne et al. 1996; Waterman and Jayne 2011) and is closely associated with the state of the KET (Qiu and Chen 2005, 2010; Wu et al. 2021; Qiu and Chen 2010; Wu et al. 2021). In addition, the winter cold air outbreaks from the Asian continents may result in significant surface heat loss from the warm KET region. This heat loss induces deep mixing through convective instability, forming a homogeneous and low stratification water mass known as subtropical mode water (STMW) (Hanawa and Talley 2001). The STMW is subducted in the SRG's vicinity and transported southeast to the southwest along subsurface isopycnals, driven mainly by the subtropical gyre.

The Kuroshio system plays a key role in the ocean ecosystem, weather, and even climate, primarily due to its significant heat transport and air–sea interaction (e.g., Small et al. 2008). Understanding the future changes under global warming scenarios is essential. Both observation and reanalysis of sea surface temperature (SST) suggested that the Kuroshio has strengthened in the twentieth century, and the KET has shifted poleward due to the change of wind stress curl (WSC) (Wu et al. 2012; Yang et al. 2016). Recently, Sasaki and Umeda (2021) confirmed that the twentieth-century SST warming tendency in the East China Sea (ECS) was caused by the accelerated Kuroshio advection. However, it is challenging to identify whether the trend is a consequence of anthropogenic forcing or natural variability due to the lack of long-term observation (e.g., Seager et al. 2001; Qiu and Chen 2010; Wang et al. 2016; Yang et al. 2016). Additionally, the associated velocity changes among different reanalysis products show large discrepancies (Yang et al. 2016), complicating the analysis of future Kuroshio changes.

Furthermore, there is still disagreement regarding the future changes of Kuroshio and the dominant mechanisms. Some studies focusing on the Kuroshio southeast of the Japanese coast (JP-Kuroshio) have proposed the occurrence of a negative midlatitude WSC tendency, potentially driven by a positive El Niño–Southern Oscillation (ENSO) or positive Arctic Oscillation (AO)–related signal. These changes lead to a northward migration and strengthening of westerlies, resulting in the acceleration and poleward shift of the KET associated with an enhanced SRG (Sakamoto et al. 2005; Sato et al. 2006; Cheon et al. 2012; Yang et al. 2016; Sen Gupta et al. 2021). However, Yamanaka et al. (2021) showed that these changes are insignificant when analyzing the Kuroshio net transport along 137°E where the flow begins to turn eastward. The uncertainty primarily comes from the substantial variance among ensemble

---

Supplemental information related to this paper is available at the Journals Online website: https://doi.org/10.1175/JCLI-D-24-0095.s1.

Corresponding author: Yu-Heng Tseng, tsengyh@ntu.edu.tw

DOI: 10.1175/JCLI-D-24-0095.1

models. Moreover, according to the Sverdrup theory, Zhang et al. (2017) argued that the acceleration of the JP-Kuroshio is influenced not only by the WSC but also by the intensified ocean stratification through the PV conservation. Besides, the stratification can also enhance the eddy kinetic energy (EKE) in the downstream KET, which can speed up the SRG. Recently, Peng et al. (2022) also suggested that the strengthened stratification enhances the entire upper subtropical gyre in their idealized experiments.

In contrast to the JP-Kuroshio, the future projected Kuroshio in the ECS (ECS-Kuroshio) may be overall decreased due to the positive subtropical WSC change (Cheon et al. 2012; Sen Gupta et al. 2021). However, studies have indicated that the speed in the upper layer of Kuroshio may be increased (Chen et al. 2019; Sen Gupta et al. 2021). Chen et al. (2019) conducted idealized ocean general circulation model (OGCM) experiments based on phase 5 of Coupled Model Intercomparison Project representative concentration pathway 4.5 scenario. They found that the warmer SST influenced the STMW temperature through vertical mixing, which was then transported to the east of Kuroshio along isopycnals. This process enhanced the upper-layer velocity of Kuroshio by baroclinicity, suggesting the dominant role of surface warming on the future Kuroshio change in the ECS. Chen et al. (2019) and Peng et al. (2022) further confirmed that the warmer SST could accelerate the upper layer of the Kuroshio while decelerating it below the thermocline.

In the northwestern Pacific, the presence of two major eddy-rich regions east of Taiwan and the KET (driven mainly by strong velocity shear and surface wind) can also affect the Kuroshio system significantly (e.g., Small et al. 2008; Kida et al. 2016; Chow et al. 2017; Chang et al. 2018). However, most OGCMs today cannot fully resolve these mesoscale eddies due to their limited spatial resolution (~1° × 1°). The lack of mesoscale eddies may potentially relate to the common northward overshoot bias of Kuroshio separation latitude in these coarse resolution OGCMs compared with observation (e.g., Hurlburt et al. 1996; Choi et al. 2002; Qiu et al. 2015; An et al. 2023), not to mention that the large meander state of Kuroshio along the south Japanese coast cannot be fully resolved where mesoscale eddies occur extensively (Tseng et al. 2012). Besides, Ma et al. (2016) proposed that, without the feedback between ocean mesoscale eddies and atmosphere, the KET mean flow will be less energetic, unstable, and shifted northward.

Based on reanalysis products and observation, Hu et al. (2020) suggested that the intensified wind work, attributed to increased greenhouse gas emission and the Pacific decadal oscillation, substantially enhanced the kinetic energy (KE) anomaly within the upper 2000 m of the ocean from 1990 to 2013, particularly in the tropical region. In addition, satellite-derived sea levels over the last three decades indicated an increase in EKE within the KET alongside a poleward shift but characterized by an unclear trend, which might be attributed to the substantial interannual variability and a cancellation effect (EKE increases and decreases offset within a fixed KET domain compared with climatology; Martínez-Moreno et al. 2021). The uncertainties among these studies likely stem from the data resolution or dynamics of ocean processes at different depths. The limited available observation still makes it inconclusive to ascertain the impact of global warming on the Pacific.

While the impact of global warming on the Kuroshio change under global warming has been extensively studied, a consensus regarding its change and underlying causes remains elusive. Several studies have separately investigated the JP-Kuroshio and ECS-Kuroshio, focusing on either the upper ocean or the entire column. Furthermore, these studies use a range of models and different future warming scenarios, yet the role of eddies in driving changes in the Kuroshio has not been carefully examined.

This study aims to investigate changes and the underlying physical mechanisms of the Kuroshio and KET under future warming scenarios. Section 2 outlines the methodology. Section 3 conducts a comparative analysis between low- and high-resolution CMIP6 models. In section 4, similar to Chen et al. (2019), an OGCM driven mainly by future surface wind and SST forcing is performed to assess the underlying dynamics. Finally, in section 5, we compare differences within each segment of the Kuroshio and between the simulations of different models while also addressing the mechanisms of the Kuroshio system under global warming.

2. Methodology

a. CMIP6

In this study, we use 33 state-of-the-art CMIP6 model results featuring various spatial resolutions (Table 1). Only the r1i1p1f1 experiment from each model is used to ensure the same control simulation across all models. The most extreme future warming scenario, SSP5-8.5, is chosen for our analysis. For the ensemble analysis, we categorize the CMIP6 models into two groups based on spatial resolution of the ocean model: low resolution (LR, ~1° × 1°) and high resolution (HR, <0.5° × 0.5°). Thus, the HR models include AWI-CM1-1-MR, CNRM-CM6-1-HR, GFDL-CM4, HadGEM3-GC31-MM, and MPI-ESM1-2-HR. The classification depends on whether the eddies in the models are parameterized or partially resolved (eddy permitting). The eddy-permitting models are typically characterized by grid sizes ranging between 0.1° and 1°, which can reasonably simulate incomplete eddy characteristics (Delworth et al. 2012; Kirtman et al. 2012; Hallberg 2013). We note that the Gent–McWilliams (GM) parameterization (Gent and Mcwilliams 1990), which is often used to parameterize mesoscale eddies in coarse resolution models, is not used in any HR models in this study, except for MPI-ESM1-2-HR. All data are interpolated to a spatial resolution of 0.25° × 0.25°, the highest ocean resolution used in the CMIP6.

b. Sensitivity experiments

Global Taiwan multiscale community ocean model (TIMCOM) is an OGCM that includes the Los Alamos Sea Ice Model, version 4 (CICE4; Hunke et al. 2017), with 1° nominal horizontal resolution and 55 *z*-coordinate levels

TABLE 1. Nominal horizontal resolution (Res.) and vertical levels in the ocean component of CMIP6 models. The use of GM parameterization is labeled as ○ (Gent and Mcwilliams 1990). Five HR models are marked with stars.

Model name	Res. × layers	GM
ACCESS-CM2	1° × 50	○
ACCESS-ESM1-5	1° × 50	○
AWI-CM1-1-MR*	0.25° × 46	×
BCC-CSM2-MR	1° × 40	○
CAMS-CSM1-0	1° × 50	○
CAS-ESM2-0	1° × 30	○
CESM2	1° × 60	○
CESM2-WACCM	1° × 60	○
CIESM	1° × 60	○
CMCC-CM2-SR5	1° × 50	○
CMCC-ESM2	1° × 50	○
CNRM-CM6-1	1° × 75	○
CNRM-CM6-1-HR*	0.25° × 75	×
CNRM-ESM2-1	1° × 75	○
CanESM5	1° × 45	○
CanESM5-CanOE	1° × 45	○
EC-Earth3	1° × 75	○
EC-Earth3-CC	1° × 75	○
FGOALS-g3	1° × 30	○
FIO-ESM-2-0	1° × 60	○
GFDL-CM4*	0.25° × 75	×
GISS-E2-1-G	1° × 40	○
HadGEM3-GC31-LL	1° × 75	○
HadGEM3-GC31-MM*	0.25° × 75	×
IPSL-CM6A-LR	1° × 75	○
MIROC6	1° × 63	○
MIROC-ES2L	1° × 63	○
MPI-ESM1-2-HR*	0.4° × 40	○
MPI-ESM1-2-LR	1° × 40	○
MRI-ESM2-0	1° × 61	○
NESM3	1° × 46	○
TaiESM1	1° × 60	○
UKESM-0-LL	1° × 75	○

(Tseng et al. 2022). The horizontal grid is 1.125° zonally and varies from approximately 0.3° on the equator to about 0.9° in the high latitude. The vertical grid is linear-exponentially stretched from 10 m at the surface to 500 m at the seafloor. The TIMCOM model employs a fourth-order-accurate spatial numerical scheme, combining Arakawa A and C grids. Temporal integration is achieved through a modified Robert–Asselin–Williams filtered leapfrog scheme (Williams 2009; Young et al. 2014). The vertical mixing is based on the K-profile parameterization (Large et al. 1994) with a critical Richardson number of 0.3. Mesoscale eddies are parameterized by the Gent–McWilliams parameterization (Gent and Mcwilliams 1990). The horizontal diffusivity coefficient is set to 3000 $\mathrm{m}^2\ \mathrm{s}^{-1}$ within the surface diabatic layer. This diffusivity diminishes as depth increases, ultimately reaching zero at the seafloor. More model details are provided in Tseng et al. (2022).

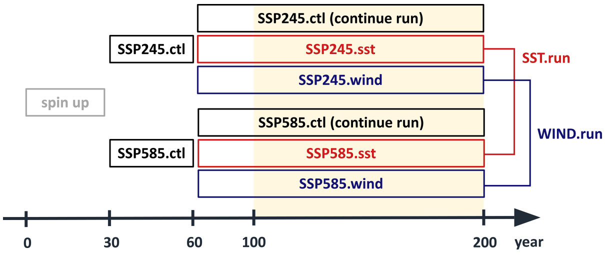

FIG. 1. Schematic of the global ocean model experiment design.

Similar to Chen et al. (2019), the sensitivity experiments are designed to investigate the individual impact of SST and wind forcings on the Kuroshio (Fig. 1). The model is initially forced by climatological Coordinated Ocean-Ice Reference Experiments phase II (CORE-II) forcing (Large and Yeager 2009) for 30 years to spin up the circulation. Subsequently, the model is driven by the annually cycled SST and wind fields derived from the mean of the first 30 years (2015–44) of the TaiESM1 output within the two future warming scenarios (SSP2-4.5 and SSP5-8.5). It is important to note that all other forcings remain consistent with the previous spinup run. These two distinct runs, denoted as ssp245.ctl and ssp585.ctl, respectively, are designated as control runs designed to replicate the specific forcings in each future warming scenario (Fig. 1). Finally, from year 60 to year 200, three sensitivity experiments are proposed: 1) continuation of the above two control runs; 2) applying only the SST forcing from the last 30 years (2070–99) of the TaiESM1 future warming scenarios, with all other forcings, including wind, remaining the same as the control run (SST.run), and 3) applying only the surface wind forcing from the last 30 years of the TaiESM1 future warming scenarios, with all others, including SST, remaining the same as the control run (WIND.run). In summary, only the net surface heat flux is changed in the SST.run, while only the momentum flux is changed in the WIND.run. Although all forcings are applied globally, the analyses in this study focus on the northwestern Pacific. The annually cycled SST or wind forcing is used in this study to reduce the uncertainty stemming from atmospheric internal variability (Seager et al. 2001; Qiu and Chen 2010; Yang et al. 2016). The last 100 years of quasi-steady equilibrium are analyzed.

For the SST forcing scheme, SST is strongly restored toward the SST field in the TaiESM1 future warming scenario through the net surface heat flux correction Q, depending mainly on the difference between prescribed and simulated SST:

$$Q = \frac{dQ}{dt}(\mathrm{SST}_{\mathrm{TaiESM1}} - \mathrm{SST}_{\mathrm{model}}),$$

$$\frac{dQ}{dt} = C_P\rho\frac{dz}{dt}, \tag{1}$$

where $\mathrm{SST}_{\mathrm{TaiESM1}}$ is the annually cycled SST from the TaiESM1 future warming scenario, $\mathrm{SST}_{\mathrm{model}}$ is the TIMCOM simulated SST, C_P is the seawater heat capacity, and ρ is the seawater density. The dQ/dt is a coefficient set to 480 $\mathrm{W\ m^{-2}\ K^{-2}}$, which is equivalent to a restoring time scale of 5 days for a 50-m mixed-layer depth. Note that the salinity remains unconstrained, implying that changes in evaporation–precipitation ($E - P$) may occur due to surface warming.

In the wind forcing run, the 10-m wind is applied based on the CORE-II formulation. However, CMIP6 standard output does not provide 10-m zonal and meridional wind components;

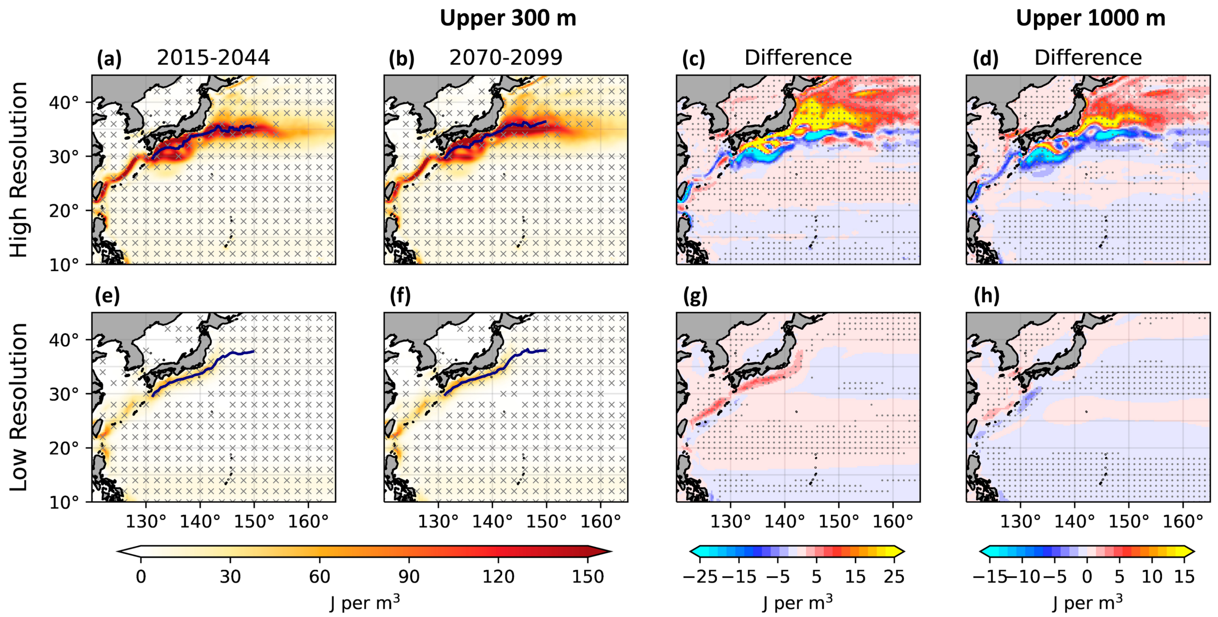

FIG. 2. (a) The 2015–44 ensemble mean of upper 300-m KE for HR models. (b) As in (a), but for 2070–99. (c) The difference between (b) 2070–99 and (a) 2015–44. (d) As in (c), but for the upper 1000-m difference. The blue lines represent the ensemble mean KET axis defined by the maximum current speed in each longitude. (e)–(h) As in (a)–(d), but for LR models. Crosses indicate areas where the signal-to-noise ratio is greater than 1 ("signal" is defined as the mean of all CMIP6 models, and "noise" is defined as the deviation of each model from the mean). Dots indicate areas where over 80% of model members agree on the sign of the differences.

instead, it offers 10-m wind speed. To derive the 10-m wind direction, we use the 6-hourly wind field data at the bottom of the pressure coordinate.

3. Change of Kuroshio in the CMIP6

a. *Kinetic energy and meridional transport*

Previous studies have suggested that the response of the Kuroshio to global warming varies with depth (Chen et al. 2019; Sen Gupta et al. 2021; Peng et al. 2022). To investigate this, we examine the spatial pattern of KE associated with the Kuroshio under the SSP5-8.5 future warming scenario at different depths (Fig. 2). We focus on the upper 300 and 1000 m using the ensemble of CMIP6 models, specifically the mean states for the initial and final 30 years of the warming projection, spanning from 2015 to 2099. Thirty-year average is enough to exclude the impacts of decadal variability, which represents a significant signal in KET region (Lin et al. 2020; An et al. 2023). The difference between these two time periods (the latter subtracted from the former) provides insight into the response to warming.

The ensemble mean of Kuroshio path in the LR ensemble (Figs. 2e,f) overshoots northward by approximately 3°. In addition, the KE of the main current is significantly lower compared to the HR ensemble (as depicted in Figs. 2a,b), and the KET is too weak to be detected. These discrepancies are common biases that tend to occur when eddies are not adequately resolved (e.g., Hurlburt et al. 1996; Choi et al. 2002; Qiu et al. 2015). Furthermore, the ECS-Kuroshio axis shifts further east in the LR ensemble compared to the HR ensemble and observational data. This shift is expected and can be attributed to the poorly represented topography of the Ryukyu Island chain in the LR models (Tseng et al. 2016).

Based on the KE change in the HR ensemble (Figs. 2c,d), we observe that the JP-Kuroshio and KET experience enhancements in both upper 300 and 1000 m, while the ECS-Kuroshio experiences a slight decrease. Notably, the KET axis shifts poleward by approximately 0.6° (Fig. 2b). On the other hand, within the LR ensemble, the entire Kuroshio path shows a marginal increase in the upper 300 m, and the meridional shift of the KET axis is less pronounced, at approximately 0.2° (Figs. 2f,g). However, in the upper 1000 m, a more distinct KE decline is observed in the ECS-Kuroshio region, particularly around the Ryukyu Island chain, while the JP-Kuroshio experiences little change (Fig. 2h). In other words, the KE of the ECS-Kuroshio increases in the upper 300 m and slightly decreases below, suggesting a baroclinic change in the LR ensemble. These differences between the LR and the HR ensembles indicate that the external atmospheric forcing or the internal ocean dynamic may differ between the two ensembles under the future warming scenario.

While the velocity or KE indicates the strength of Kuroshio, meridional transport better quantifies the poleward heat transport from low latitudes. Figure 3 compares the upper 300-m barotropic streamfunction (BSF) between the LR and HR ensembles. The mean transport of the ECS-Kuroshio during 2015–44 is approximately 20 Sv (1 Sv ≡ 10^6 m^3 s^{-1}) in both LR and HR ensembles (Figs. 3a,e). However, the LR ensemble shows a weaker zonal gradient compared to the HR

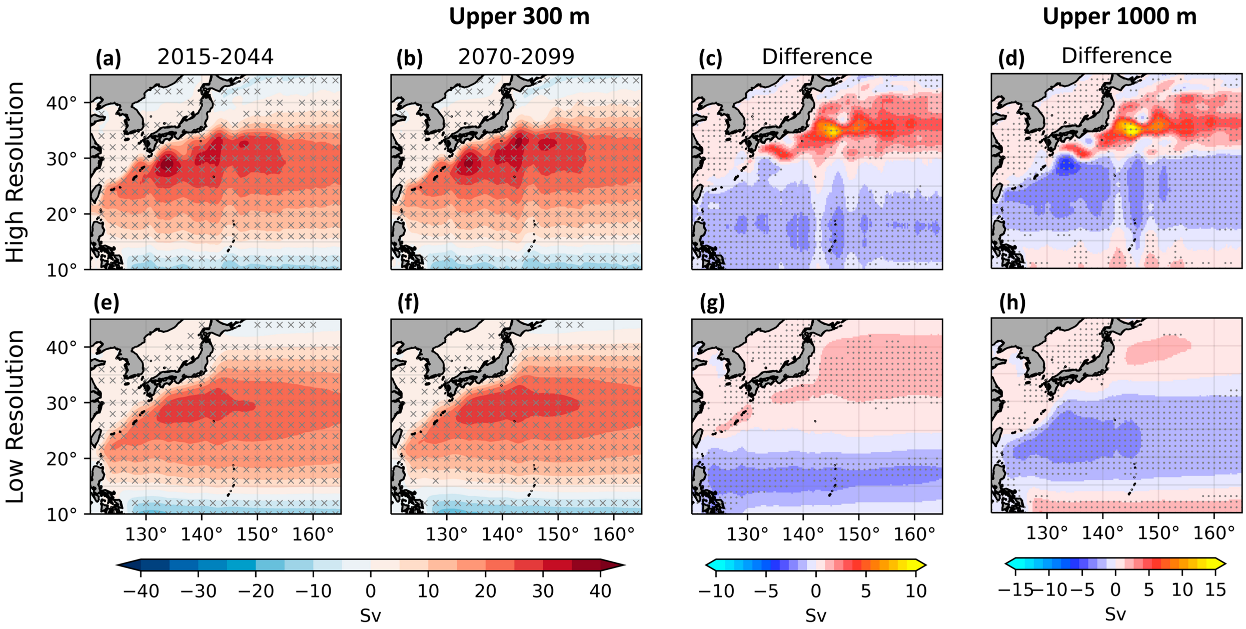

FIG. 3. As in Fig. 2, but for the BSF.

ensemble, suggesting an underestimated KE (i.e., meridional velocity) and a broader Kuroshio band. Regarding the mean transport in the JP-Kuroshio, the corresponding mean transport of the SRG and the KET can reach approximately 35 Sv in the upper 300 m in the HR ensemble, significantly higher than the modeled 25 Sv in the LR ensemble. We also note that the SRG in the LR ensemble is weak and broad south of Japan while two major anticyclonic gyres are formed in the HR ensemble: one to the south and the other to the east of Japan, similar to Cheon et al. (2012). These differences are likely attributed to the impacts of mesoscale eddies (Qiu and Chen 2010).

Overall, the changes in BSF under the future warming scenario are closely related to those in KE (Figs. 3c,d,g,h). However, we can observe an anticyclonic circulation change surrounding the Ryukyu Island chain (Fig. 3g), which is not

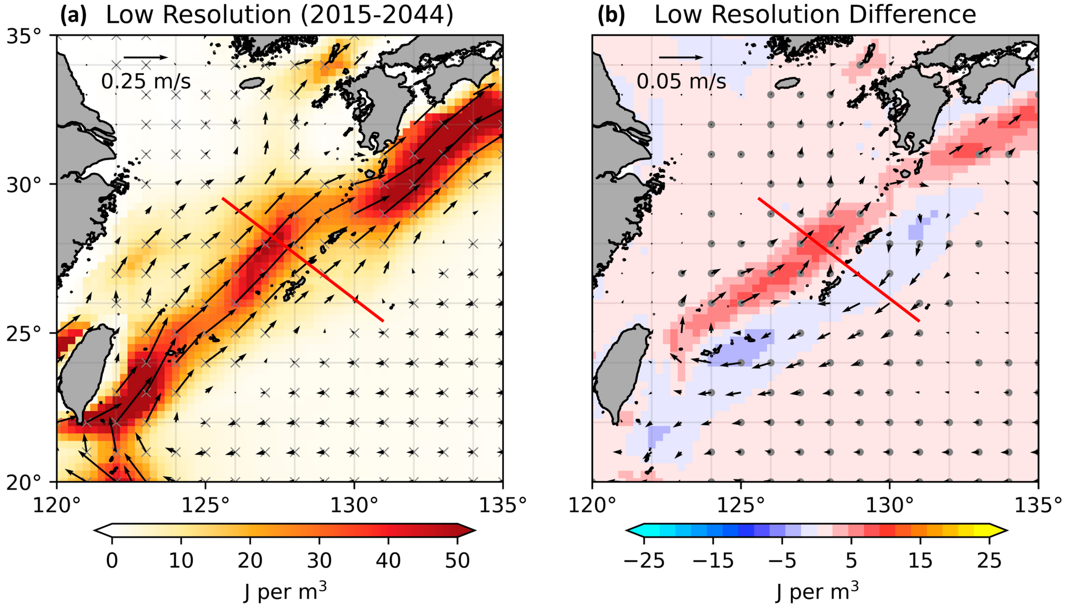

FIG. 4. (a) The 2015–44 ensemble mean of upper 300-m current velocity vector and KE (shading). (b) The difference between 2070–99 and 2015–44. PN section is shown as a red solid line, spanning from (29.6°N, 125.5°E) to (25.3°N, 131°E). The significant test is the same as that in Fig. 2.

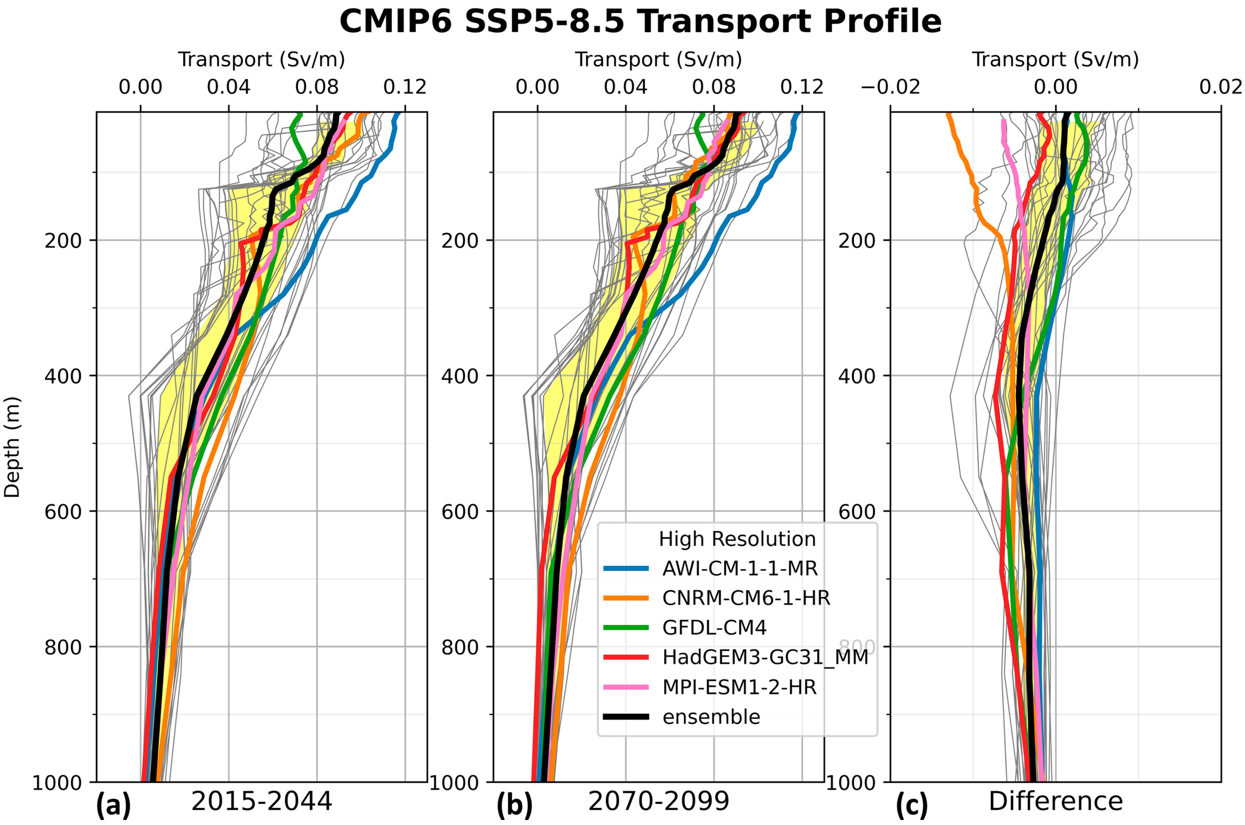

FIG. 5. (a) The 2015–44 mean of meridional transport profile across the PN section. (b) As in (a), but for 2070–99. (c) The difference between (b) 2070–99 and (a) 2015–44. Colored, gray, and black lines indicate HR models, LR models, and all 33 model ensembles, respectively. Yellow shading indicates the interquartile range.

apparent in the change of KE pattern. The current velocity vectors (Fig. 4) further confirm a more substantial positive KE change on the west side compared to the negative change on the east of the Ryukyu Island chain. The asymmetry of the KE change is likely due to the nonlinear term, with the higher mean velocity on the west. In other words, the ECS-Kuroshio not only accelerates along its main axis but also concurrently narrows, resulting in the pattern change between the KE and transport tendency.

The meridional transport per unit thickness in the central East China Sea (PN section), indicated in Fig. 4, shows a clear vertical change in the ECS-Kuroshio (Fig. 5). As depicted in Figs. 5a and 5b, the simulated mean transport in the upper layer shows significant variability among the LR models, with a range of approximately 0.08 Sv m^{-1}. The maximum transport is nearly triple the minimum value, highlighting the challenges associated with an accurate representation of the ECS-Kuroshio dynamics within climate models. However, no substantial difference in transport is observed between the HR and the LR model groups throughout the entire column, consistent with the findings in Fig. 3.

In the future 2070–99 warming scenario, the overall transport of the upper 200 m remains nearly constant due to the anticyclonic change around the Ryukyu Island chain (Fig. 5c), as discussed in Fig. 4b. However, a decreasing transport trend is observed in the deeper layer, consistent with the findings in Figs. 3d and 3h. The transport change in the upper layer demonstrates a scattered distribution across models. Notably, among the five HR models, three show changes falling below the lower quartile. Except for GFDL-CM4 and AWI-CM-1-1-MR, the HR models lack the baroclinic change shown in the ensemble and most LR models, indicating that the consistent baroclinic change is less pronounced in the HR models.

According to the Sverdrup theory, the subtropical gyre in the northwest Pacific is mainly driven by negative WSC associated with the Pacific subtropical high. Consequently, changes in WSC, including the Kuroshio, can directly affect the gyre speed. We note that the negative WSC weakens southward of 30°N and strengthens northward, thus forming a dipole-like pattern change (Fig. A1 in the appendix) in the future warming scenario. This suggests a poleward shift of midlatitude zero WSC line (i.e., midlatitude westerly wind) due to potential Hadley cell expansion (e.g., Lu et al. 2007; Davis and Birner 2022). These WSC changes are more pronounced in the HR ensemble than in the LR ensemble. The dipole distribution in WSC change aligns with the spatial pattern observed in the KE and meridional transport, delineating two distinct regions defined earlier: ECS-Kuroshio and the JP-Kuroshio. However, this pattern is not seen in the LR ensemble in the upper 300 m.

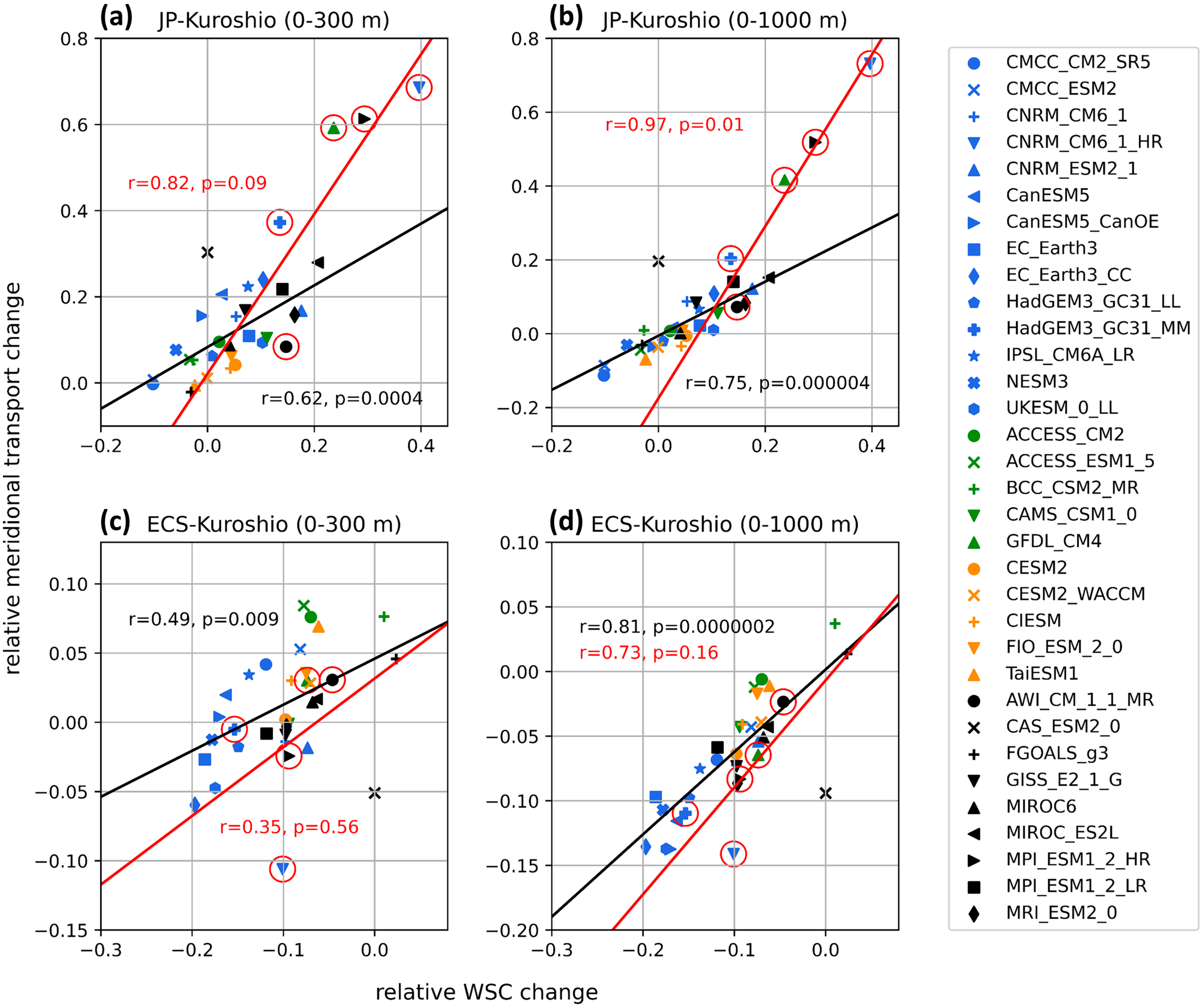

FIG. 6. (a) Relationship between the relative meridional transport changes in the upper 300-m JP-Kuroshio and the relative WSC change. WSC change is defined as the areal mean within the region (140°E–80°W, 31°–42°N). (b) As in (a), but for the upper 1000 m. (c),(d) As in (a),(b), but for ECS-Kuroshio. WSC change is defined as the areal mean within the region (120°E–80°W, 20°–31°N). Blue, green, orange, and black markers represent ocean models based on NEMO, MOM, POP, and others, respectively. Red circles indicate HR models. Red and black lines indicate the regression line of HR and LR models, respectively.

We further address the response of meridional transport changes in the Kuroshio to WSC using the scatterplots. The calculation of JP-Kuroshio and ECS-Kuroshio transports mainly follows the methodology of Sen Gupta et al. (2021) (WSC regions of JP and ECS are defined in Fig. A1, in the appendix). First, the Kuroshio mask is defined as grids where the kinetic energy exceeds 5 J m^{-3} (Fig. A3, in the appendix). Meridional transport is then calculated for each latitude within this mask. Finally, a meridional weighted mean is computed for each latitude range: 20°–31°N for ECS-Kuroshio and 31°–42°N for JP-Kuroshio. Note that the KET region to the east of 145°E is excluded. Given the substantial variation in the mean meridional transport of the Kuroshio across different models (HR ensemble showing significantly higher intensity than LR ensemble for JP-Kuroshio), our analysis focuses on relative changes in relationship to the individual mean transport.

Relationship between WSC and transport change is statistically significant in the upper 1000-m ECS-Kuroshio (Fig. 6d). The relationship between WSC and transport is consistent regardless of the specific ocean models used (ocean models are grouped into NEMO, MOM, POP, and others as different colored markers). Moreover, those HR markers labeled with red circles, except CNRM-CM6-1-HR, also share nearly the same regression line with LR, suggesting that the difference of ECS-Kuroshio change among CMIP6 models, including HR, may be attributed to variations in atmospheric wind magnitude.

In the JP-Kuroshio, the relationship between WSC and transport change remains significant in both depth ranges (Figs. 6a,b). Notably, the transport of HR models is more sensitive to WSC changes than that of LR models in both depths, indicated by the steeper regression line in HR models. This suggests that the eddy-resolved dynamics may contribute further to the

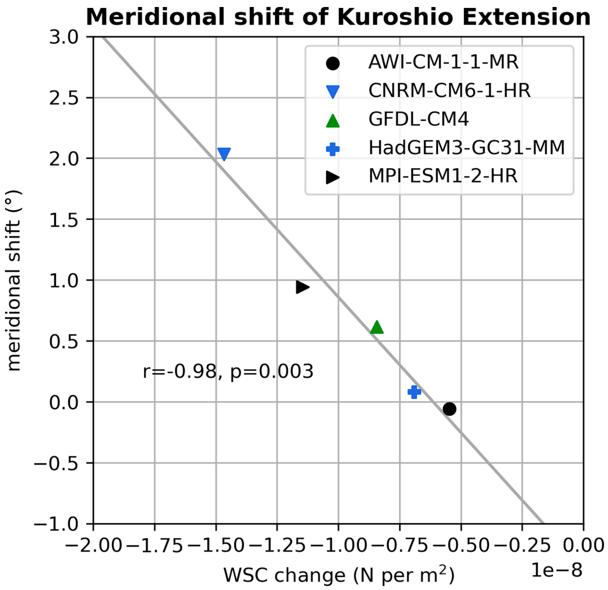

FIG. 7. Scatterplots of WSC change against the meridional shift of the KET. The meridional shift is defined as the mean location shift of the KET axis within 142.5°–150°E.

HR models during future warming scenarios. Moreover, the meridional shift of KET is also significantly proportional to the WSC changes in HR models as expected (Fig. 7), suggesting the dominant role of WSC change on the poleward shift of KET (Wu et al. 2012; Yang et al. 2016). Note that the meridional shift of KET in the LR models is not shown because their KET axis cannot be adequately resolved and defined.

b. *Vertical thermal structure*

In the SSP5-8.5 scenario, the SST warming patterns exhibit subtle differences between the LR and HR models (Fig. A2 in the appendix). Both resolutions show evident impacts of Arctic amplification, characterized by an intensified SST warming as one moves poleward. These warming patterns qualitatively correspond to the Kuroshio recirculation. However, the Kuroshio likely transports less warming seawater from the tropics to the extratropic in the HR model ensemble, resulting in a pattern of weaker SST change. Chen et al. (2019) argued that, rather than the primary impact of wind stress, the strength of the Kuroshio in the upper layer is predominantly affected by the propagation of warm STMW generated by warm SST around the KET region. This suggests that the Kuroshio change can also be attributed to the SST change pattern through the STMW. In this study, STMW is identified based on the typical low PV criterion as follows:

$$\mathrm{PV} = (\zeta + f)\frac{1\partial\rho}{\rho\partial z}. \tag{2}$$

Vertical sections at 165°E (P13) and 26.75°N (center of the ECS-Kuroshio) show the location and characteristics of STMW (Fig. 8). During 2015–44, STMW primarily occupies the depth range of approximately 100–400 m along the P13 sections, where the slight vertical density gradient enhances effective mixing of water masses (Figs. 8a,e). In the HR ensemble, the bottom of STMW is located at greater depth compared to the LR ensemble. However, the PV values are higher in the HR, suggesting that, while the mixing depth extends further in the HR, the mixing itself is less uniform

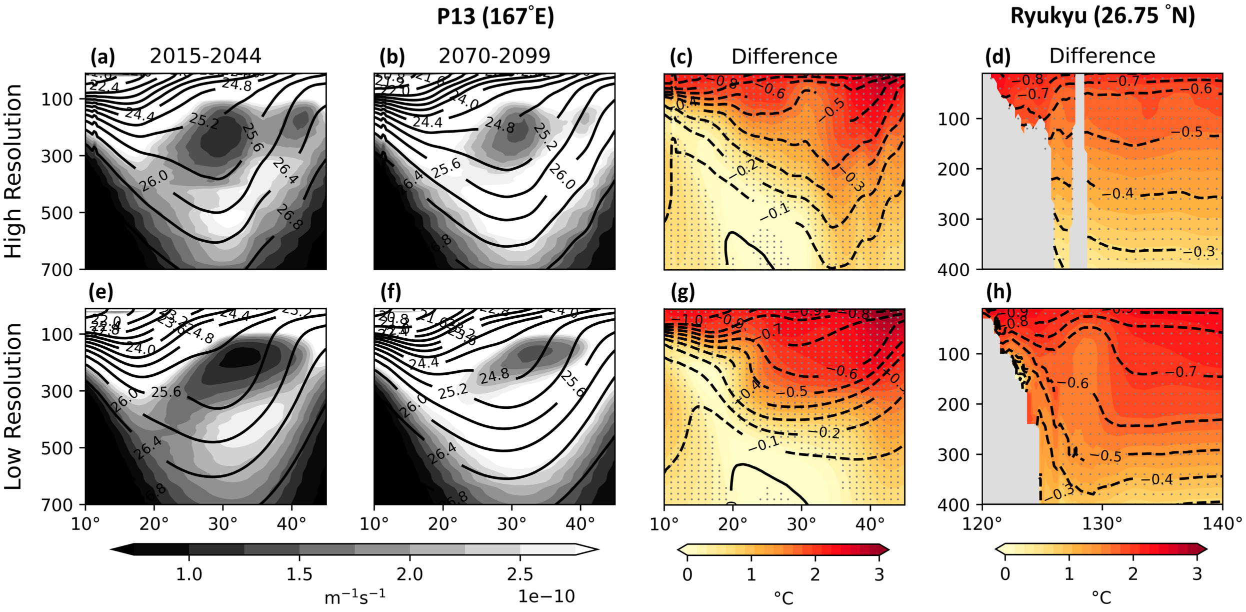

FIG. 8. (a) The 2015–44 ensemble mean of potential density (contour) and PV (shading) for HR models in the meridional section along P13 (165°E). (b) As in (a), but for 2070–99. (c) The difference between (b) 2070–99 and (a) 2015–44 of potential density (contour) and potential temperature (shading). (d) As in (c), but for the zonal section across the ECS-Kuroshio (26.75°N). (e)–(h) As in (a)–(d), but for LR models. Dots indicate areas where over 80% of model members agree on the sign of the trends.

compared to the LR. Additionally, given the southward subduction of STMW below the KET (Hanawa and Talley 2001; Douglass et al. 2013), the northern boundary of STMW is situated at 35°N in the HR, while it overshoots to 40°N in the LR. During 2070–99, the bottom of STMW becomes shallower, accompanied by an increase of PV due to enhanced stratification from surface heating. This increased stratification hinders seawater from mixing effectively into deeper levels in both sections (Figs. 8b,f). Similar results are also shown in Wang et al. (2013).

The density changes under future warming scenarios are primarily influenced by temperature changes (Figs. 8c,g), which is also supported by Zhang et al. (2017). Despite the decrease in STMW transport in 2070–99, the LR ensemble continues to exhibit a subsurface warm water pattern distributed along the isopycnal from midlatitude to 20°N in the P13 section. In contrast, the HR ensemble confines the subsurface warm water to around 30°N. The warm water pattern along the sections is more likely to correspond to the STMW pattern in LR. The distinct pathways and volume of warm water between HR and LR may contribute to different mechanisms for the changes of Kuroshio under future warming scenarios.

Figures 8d and 8h show the warm water transport across the ECS-Kuroshio at 26.75°N. The LR ensemble shows a slightly less pronounced warming change at 126°–130°E, possibly attributed to changes in temperature advection. This feature is also observed in Chen et al. (2019) (their Figs. 9 and 10). In the LR, the warming east of the Kuroshio is more pronounced compared to the HR, as supported by the P13 section, where the warm water associated with the STMW is more prominent in the LR. While these heterogeneous warming patterns suggest an enhanced thermal wind relationship (e.g., Fig. S1 in the online supplemental material), further examination is required to understand the underlying causes for the differences between LR and HR.

4. TIMCOM sensitivity experiments

a. *Kinetic energy and meridional transport*

To identify the primary driver of the Kuroshio changes in future warming scenarios, we examine the impacts of wind and SST changes under SSP2-4.5 and SSP5-8.5 scenarios. In SSP2-4.5, the KE is enhanced along the entire path of Kuroshio due to the SST change (SST.run) in Fig. 9a. More intense SST warming is observed between 145° and 165°E than along the east coast of Japan (not shown). As a result, the KET region tends to shift equatorward due to the thermal wind balance.

On the contrary, the wind change simulation (WIND.run) under the SSP2-4.5 scenario (Fig. 9c) shows a dual-response pattern in the upper 300-m KE: a decrease to the south of Japan, approximately below 32°N, and an increase to the north of 32°N. This dipole-like change possibly results from the Hadley cell expansion in the projected future warming scenario (e.g., Lu et al. 2007; Davis and Birner 2022). The zero WSC line shifts poleward, resulting in a dipole-like WSC change pattern observed across all CMIP6 models (but magnitude varies among models), including TaiESM1 (Fig. A1 in the appendix).

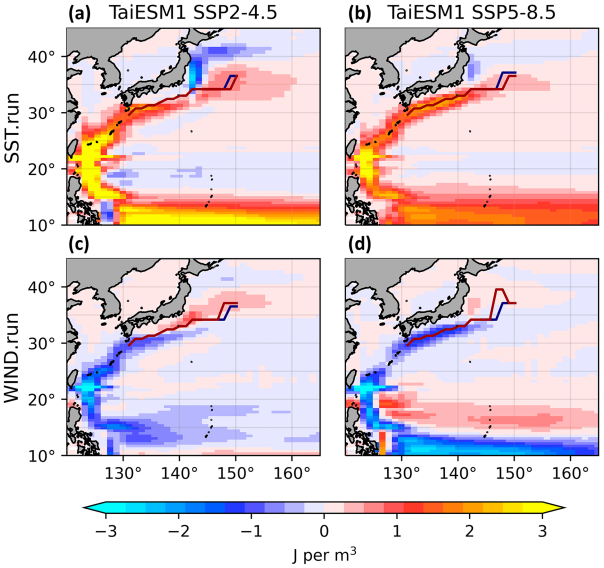

FIG. 9. The upper 300-m mean KE difference between (a) SSP245.sst and SSP245.ctl for SST change experiment (SST.run). (b) As in (a), but for the SSP5-8.5 scenario. (c),(d) As in (a),(b), but for wind change experiment (WIND.run). Blue and red lines represent the mean KET axis in the control run and SST.run (WIND.run).

While the magnitude of the KE change is more significant in the southern region than in the northern part, the distinct KE patterns suggest a northward shift of the Kuroshio along the coast of southern Japan, with an insignificant shift in the Kuroshio axis, including the KET. In short, our sensitivity studies under the SSP2-4.5 scenario indicate that the response to surface warming outweighs that to wind stress changes, emphasizing the dominant role of surface warming along the entire Kuroshio path. These findings align with previous studies of Chen et al. (2019) and Peng et al. (2022).

Similar change patterns can be found under the SSP5-8.5 scenario compared to the SSP2-4.5 scenario (Figs. 9b,d). These patterns indicate a more reduced magnitude change along the south coast of Japan in the WIND.run and a more substantial change in the SST.run under the SSP5-8.5 scenario. The magnitude of the response in the SST.run remains slightly greater along the south coast of Japan and the ECS compared to the WIND.run. This highlights the prevailing influence of surface warming in both future warming scenarios.

Figure 10a shows the mean meridional transport profiles around the Ryukyu Island chain across the PN section. The ECS-Kuroshio is predominantly concentrated above 1000 m and nearly diminishes below this depth. The depth of no motion between each experiment is nearly consistent. Moreover, the enlarged figure highlights distinct transport profiles in the upper 300 m for each experiment, suggesting that the current shear in the upper ocean is influenced by specific forcings. These results are consistent with Chen et al. (2019) and Peng et al. (2022).

The transport difference in the ECS-Kuroshio between each sensitivity test and control run is shown in Fig. 10b. In the upper 300 m, the response to the surface warming is

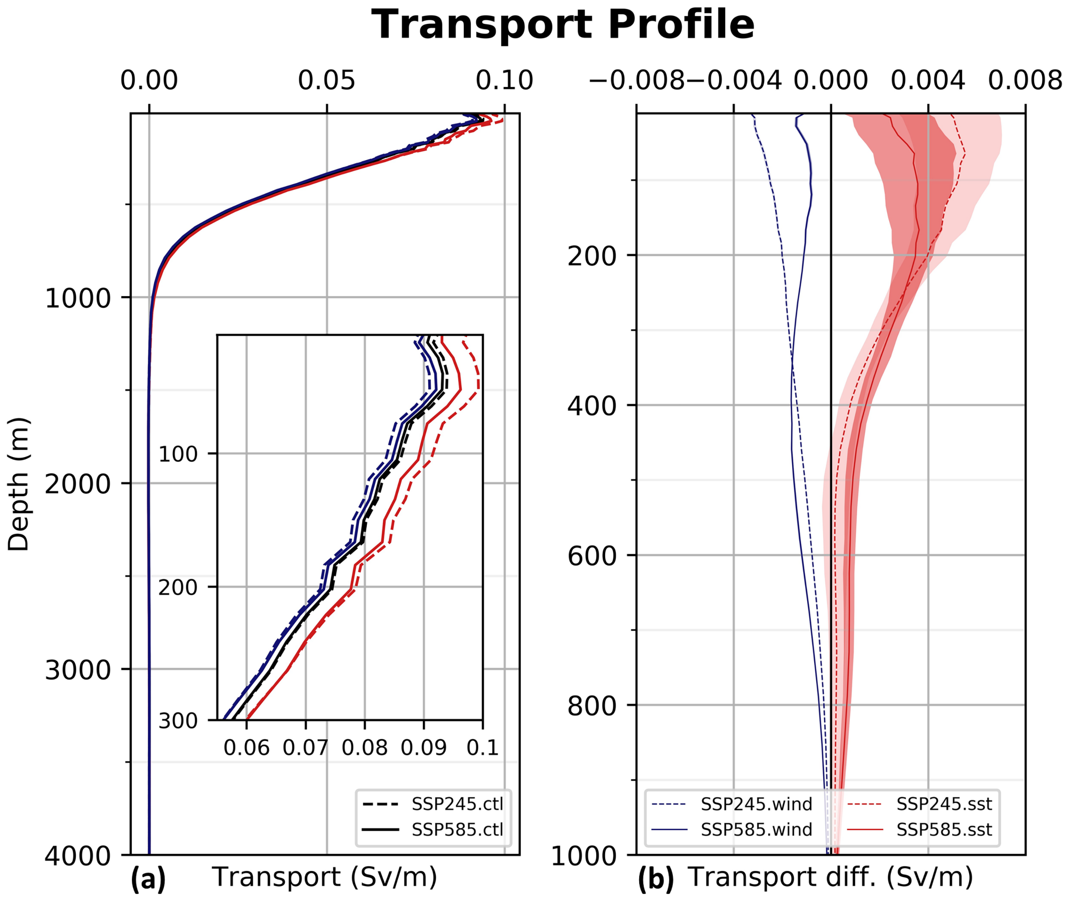

FIG. 10. (a) Mean meridional transport profiles across the PN section. The black, red, and blue lines indicate the control, SST, and wind runs, respectively. The solid (dashed) lines correspond to the SSP5-8.5 (SSP2-4.5) scenario. (b) Differences between the SST.run/WIND.run and control runs in each future warming scenario. Each color shading indicates the interquartile range of each annual mean.

particularly more significant than that to the wind change, with the most significant change occurring at around 50 m in both future warming scenarios. However, below 300 m, the impact of surface warming decreases rapidly, and the influence of wind becomes more pronounced than that of SST. The results suggest that surface warming dominates the ECS-Kuroshio change in the upper 300 m in both scenarios, while wind dominates below 300 m.

We note that the response in both WIND.run and SST.run exhibits certain variations across the SSP2-4.5 and SSP5-8.5 scenarios. Particularly, the variation spread is significantly larger in the SST.run than the WIND.run (interquartile range of each annual mean is shaded), regardless of the future warming scenarios. This is primarily attributed to substantial decadal internal variability in SST.run. Furthermore, the transport response in the SSP245.sst run exceeds that of the SSP585.sst above 200 m, suggesting stronger stratification in the SSP245.sst, contrary to our intuitive expectations. This may arise from the absence of constraints on the salinity flux, leading to increased stratification or evaporation, resulting in higher salinity that compensates for the density changes (not shown). Consequently, the density change impacts the transport response due to thermal wind balance.

b. *Vertical thermal structure*

Similar to section 3b, we further examined the vertical sections along 165°E (P13) to investigate the changes of the warming water and STMW in the SST.run. In the control run of both future warming scenarios (Figs. 11a,e), where the SST is nudged to the mean of the first 30 years of the scenario, the stratification is strong, resulting in a bottom layer of STMW less than 300 m, already shallower than current observations (Wang et al. 2013; Douglass et al. 2013; Tsubouchi et al. 2016; Wu et al. 2021). Compared to the responses of each control run, both SST.run experiments (Figs. 11b,f) show a thinner STMW with an increased PV. This suggests that the characteristics of the STMW become less pronounced, similar to the findings in CMIP6 (Figs. 8b,f). Besides, under the more severe scenario (Figs. 11f,g), the PV of the STMW exhibits a more notable increase in the SST.run. This is attributed to the intensified surface heat flux, which enhances stratification in the ocean and hinders the generation of STMW by suppressing vertical mixing.

Despite the reduced thickness of the STMW in the SST.run, we can still observe warm water patterns along 23.6–25.6 kg m^{-3}

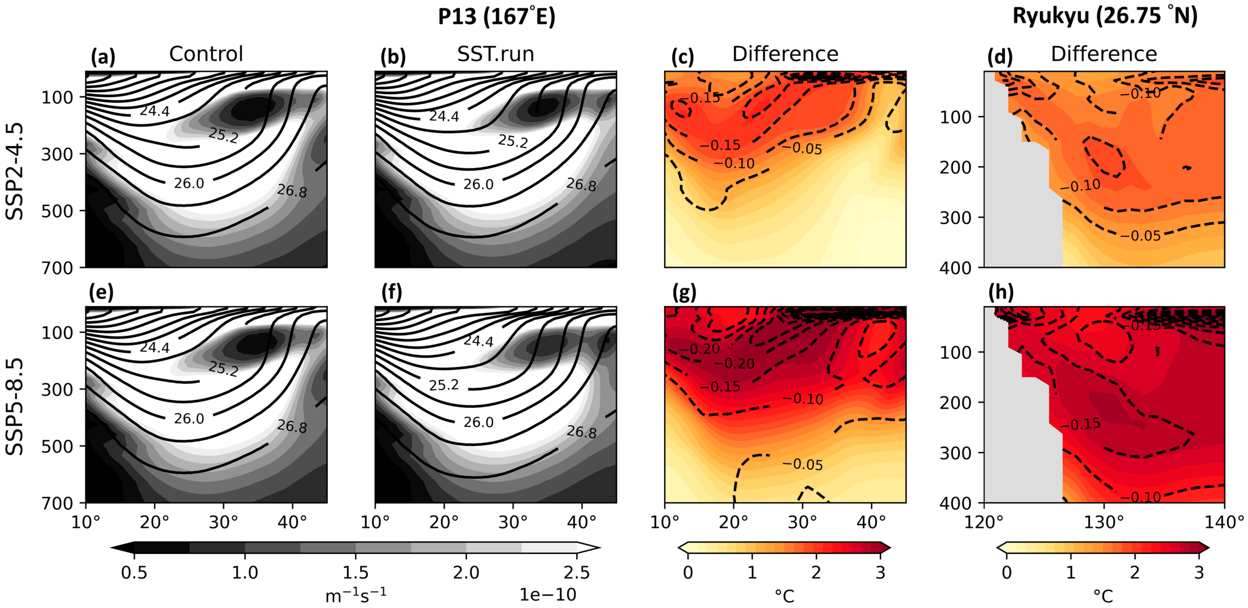

FIG. 11. The mean potential density (contour) and PV (shading) in (a) SSP245.ctl and (b) SSP245.sst in the meridional section along P13 (165°E). (c) The difference between (b) SSP245.sst and (a) SSP245.ctl. (d) As in (c), but for the zonal section across the ECS-Kuroshio (26.75°N). (e)–(h) As in (a)–(d), but for SSP5-8.5 scenario.

isopycnal, representing the primary distribution region of the STMW (Figs. 11c,g). However, this warm water distribution in both future warming scenarios differs from those in the CMIP6 LR ensemble in the tropical region (south of 20°N, Fig. 8g), suggesting that factors other than SST warming also contribute to the warm water distribution in the more complicated coupled model simulation.

Figures 11d and 11h illustrate the baroclinic changes observed in the ECS-Kuroshio. Consistent with the findings of CMIP6 (Figs. 8d,h), the distribution of warm water changes in the SST.run primarily occurs to the east of the Kuroshio in both future warming scenarios, particularly in the upper 300 m. This depth is consistent with the warming-induced changes in meridional transport, as shown in Fig. 10b. Besides, we have confirmed that the level of no motion remains nearly unchanged across all experiments (Fig. 10a). Therefore, based on thermal wind relation, an increase in the zonal density gradient enhances the northward geostrophic current. Although the magnitude of ocean warming significantly differs under different scenarios, the overall pattern of density change remains similar, indicating a comparable zonal density gradient. Consequently, the differences in Kuroshio changes between SSP585.sst and SSP245.sst are minimal. This similarity in density change can be attributed to the absence of constraints on the salinity flux, which has been mentioned in section 4a. Note that the SSP245.sst run exhibits stronger stratification than the SSP585.sst run at around 300 m depth, as illustrated in Fig. 10b.

To trace the transport of STMW along isopycnals, potential temperature and PV are interpolated to isopycnal levels at 0.1 kg m^{-3} interval from the z-coordinate depths. Given the density changes associated with ocean warming, distinct isopycnal levels are selected between SSP245.sst (SSP585.sst) and SSP245.ctl (SSP585.ctl), as per Wang et al. (2013). Based on the temperature change profile in Figs. 11c and 11g, the density change near the STMW location is approximately -0.1 kg m^{-3} in both SSP2-4.5 and SSP5-8.5 scenarios. Therefore, in the SST.run, the isopycnal is chosen to be 0.1 kg m^{-3} lighter than the control case in each respective set of isopycnal.

In the control runs (contour in Fig. 12), the low PV indicates the location and pathway of STMW. The STMW subducts near the outcrop region of the KET and subsequently advects southeast to southwest along isopycnals (Hanawa and Talley 2001; Xie et al. 2011). The pattern of warm water corresponds to the low PV region across various isopycnals and future warming scenarios, showing that the warm water originated from the sea surface indeed transports along with the STMW. Additionally, in shallower layers with densities of 24.8/24.7 kg m^{-3}, STMW propagates more directly southward (Figs. 12b,d). Hence, the STMW in these shallower layers is situated closer to the east of Kuroshio, facilitating more effective tilting of isopycnals across the Kuroshio and enhancing meridional velocity shown earlier.

In conclusion, our sensitivity experiments demonstrate that surface heating plays a pivotal role in enhancing the Kuroshio within the upper 300 m. STMW subducts along with the warm water in the KET region, moving toward the east of the Kuroshio. This results in a more tilted isopycnal across the Kuroshio and an augmented northward velocity according to the thermal wind balance. Below 300 m depth, the signal of warm STMW diminishes, and changes in wind patterns become the predominant factor in the Kuroshio's decline. This clarifies the baroclinic change observed in the ECS-Kuroshio in the LR ensemble of CMIP6. Furthermore, our analysis highlights the salinity compensation induced by surface heating is also crucial to the transport change through density structure, suggesting

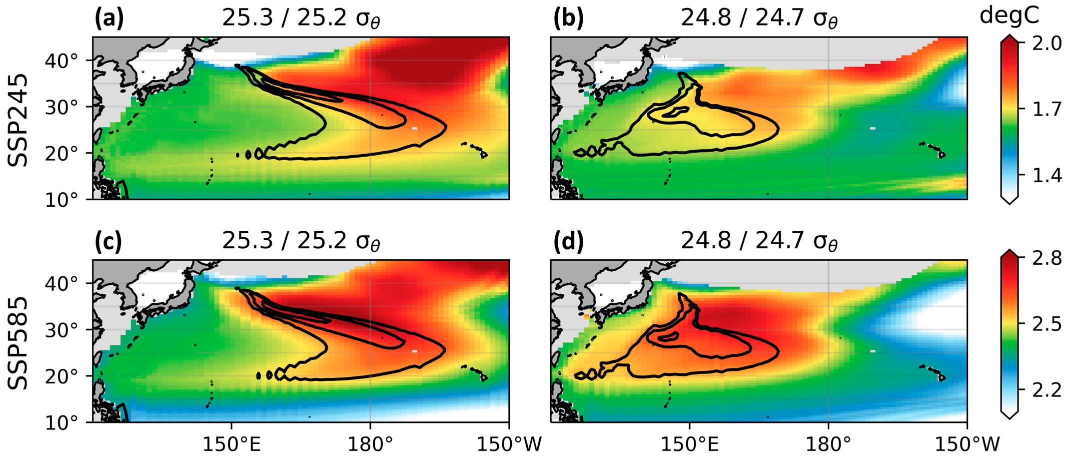

FIG. 12. (a) PV along 25.3 kg m^{-3} isopycnals in SSP245.ctl (contour, [1, 2, 3] × 10^{-10} m^{-1} s^{-1}) and potential temperature change between SSP245.sst and SSP245.ctl along 25.2 and 25.3 kg m^{-3} isopycnals, respectively (shading). (b) As in (a), but for SSP245.sst (SSP245.ctl) along 24.7 (24.8) kg m^{-3} isopycnals. (c),(d) As in (a),(b), but for SSP5-8.5 scenarios.

that the surface salinity flux may also play a role in ocean circulation under future warming scenarios.

5. Conclusions and discussion

The future changes of WBCs are influenced by many different mechanisms. Some WBCs changes are linked to interbasin exchanges, e.g., Gulf Steam (Weijer et al. 2020) and Indonesian Throughflow (Sen Gupta et al. 2016). Some others result from wind stress curl change, e.g., low-latitude WBC (Sen Gupta et al. 2012). However, compared with other WBCs, the projected Kuroshio change is more complicated due to different warming rates of surrounding water masses, leading to a distinctive baroclinic change not observed in other WBCs (Sen Gupta et al. 2021). Moreover, most OGCMs today cannot adequately resolve the mesoscale eddies due to their coarse spatial resolution. This is a major deficiency for simulating the Kuroshio, as mesoscale eddies play crucial roles in the KET, the path along the south Japanese coast, strength along the east of Taiwan, energy exchange, and so on (e.g., Hurlburt et al. 1996; Tseng et al. 2012; Chang et al. 2018). This study aims to closely investigate the underlying mechanisms that drive the changes of Kuroshio during future warming scenarios. The Kuroshio changes within the CMIP6 SSP5-8.5 scenario depend on latitudes, depths, and model resolutions, as summarized in Table 2.

In the LR ensemble, the spatial pattern of KE and transport changes in the ECS-Kuroshio within the CMIP6 ensemble can be attributed to an enhanced anticyclonic upper ocean circulation around the Ryukyu Island chain (Fig. 4). This leads to an increase in the central axis of the Kuroshio's KE while the overall transport across the circulation remains unchanged. Furthermore, the KE of ECS-Kuroshio exhibits an increase in the upper 300 m but a decrease in the upper 1000 m within the CMIP6 ensemble. Our sensitivity experiments clarify that the baroclinic change is primarily influenced by the warm STMW (Fig. 12). In the projected future warming scenario, the surface warming subducts with the STMW through mixing and transport, facilitated by the wind-driven subtropical gyre. The warm STMW contributes to elevated ocean temperature east of the Kuroshio, resulting in an increased isopycnal slope across the Kuroshio to enhance the Kuroshio. This intensification is more pronounced in the upper 300 m and surpasses the reduction caused by wind effects in both the SSP2-4.5 and SSP5-8.5 scenarios. Below 300 m, the influence of the warm STMW diminishes, and the Kuroshio changes are dominated by the impact of wind change.

However, both Chen et al. (2019) and Peng et al. (2022) argued that SST is the dominant factor throughout the entire water column, including the decrease of Kuroshio velocity between 400 and 1200 m depth. This difference could potentially

TABLE 2. Summary of different parts of Kuroshio change in CMIP6 ensembles.

	LR	HR
Upper 300 m		
JP-Kuroshio	Enhanced	Enhanced dramatically, poleward
ECS-Kuroshio	KE: Enhanced Sv: No changed	Reduced
Upper 1000 m		
JP-Kuroshio	Enhanced	Enhanced dramatically, poleward
ECS-Kuroshio	Reduced	Reduced

be attributed to the different numerical configurations. It is noteworthy that the Kuroshio changes are sensitive to the surface salinity flux in our sensitivity experiments. The impacts of salinity flux due to surface heating on the Kuroshio have not been addressed in the CMIP6 study. Further investigation of the salinity flux is required but beyond the scope of this study.

Within the JP-Kuroshio of CMIP6 ensemble, the expansion of the Hadley cell is the dominant driver for the changes of Kuroshio, observed within the upper 1000 m in both HR and LR ensembles and the upper 300 m in the HR ensemble. This expansion induces a poleward shift of the zero line for the WSC, leading to a reduction of negative WSC to the south of 30°N and an increased negative WSC to its north. As a result, the JP-Kuroshio experiences enhancement while the ECS-Kuroshio undergoes weakening according to the Sverdrup theory. The Sverdrup relation (Fig. 6) further emphasizes that the magnitude of the Kuroshio changes correlates well with the magnitude of WSC change across various ocean models. We note that only the HR ensemble has simulated a significant poleward shift of the KET in response to the Hadley cell expansion, possibly indicating the inadequate simulation of KET in the LR models. This wind-driven mechanism has been well recognized in the literature, such as Sakamoto et al. (2005) and Cheon et al. (2012).

However, our sensitivity experiments using a LR model indicate that the increase of KE within the upper 300 m, induced by surface warming, is not only limited to the ECS-Kuroshio but also along the south Japanese coast. This is also consistent with Chen et al. (2019) and Peng et al. (2022). The underlying physical process is likely linked to the warm STMW transported to the east of ECS-Kuroshio, as discussed earlier, or it may be influenced by strengthened ocean stratification, resulting in accelerated velocity through PV conservation (Zhang et al. 2017). It is noteworthy that the Sverdrup relation (Fig. 6) suggests that the JP-Kuroshio change is more sensitive to the WSC change in the HR ensemble. Furthermore, the vertical profiles (Fig. 8) show that the warm water, along with STMW, is not as prominent in the HR ensemble, which may potentially impact the physical mechanism addressed here. Therefore, further investigation is essential to determine the role of STMW or other mechanisms in strengthening the Kuroshio in the HR ensemble.

Acknowledgments. We thank the discussion and comments from Dr. Huang-Hsiung Hsu, Prof. I.-I. Lin, and Prof. Shih-Nan Chen. Constructive comments from three anonymous reviewers are truly appreciated. This work was supported by Grants 112-2119-M-865-004, 112-2611-M-002-016-MY3, and 113-2639-M-002-008-ASP, National Science and Technology Council, Taiwan. Computer resources from the National Center for High-Performance Computing (NCHC) of National Applied Research Laboratories (NARLabs) in Taiwan are appreciated.

Data availability statement. The CMIP6 data are publicly available through the portal of the U.S. Earth System Grid Federation on the page https://aims2.llnl.gov/search/cmip6/.

APPENDIX

Supplementary Differences and Mask Definition for the Response of Meridional Transport Changes

Figures A1 and A2 are the extra figures showing the ensemble differences between 2070–99 and 2015–44. Figure A3 shows the mask definition of Kuroshio based on the KE.

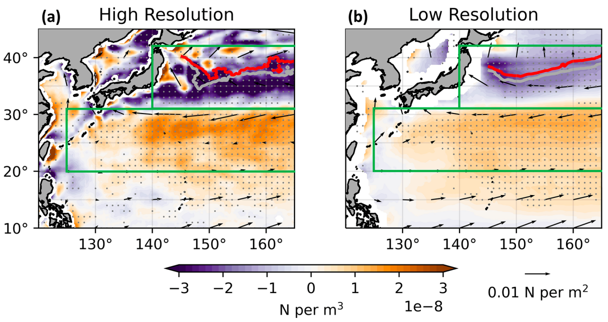

FIG. A1. The ensemble difference of wind stress vector and WSC (shading) between 2070–99 and 2015–44 for (a) HR and (b) LR models. Dots indicates areas where over 80% of model members agree on the sign of the trends. Gray and Red lines indicate the mean zero WSC line in 2015–44 and 2070–99, respectively. Green boxes indicate the locations of JP and ECS for Figs. 6 and 7.

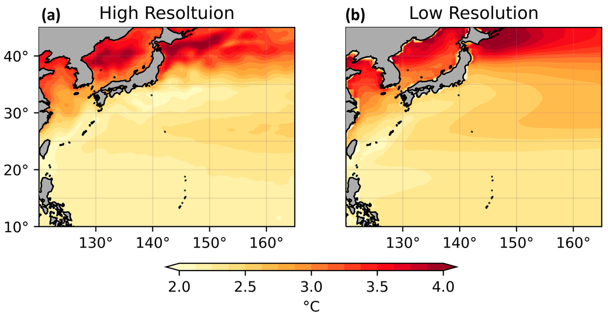

FIG. A2. The ensemble difference of SST between 2070–99 and 2015–44 for (a) HR and (b) LR models.

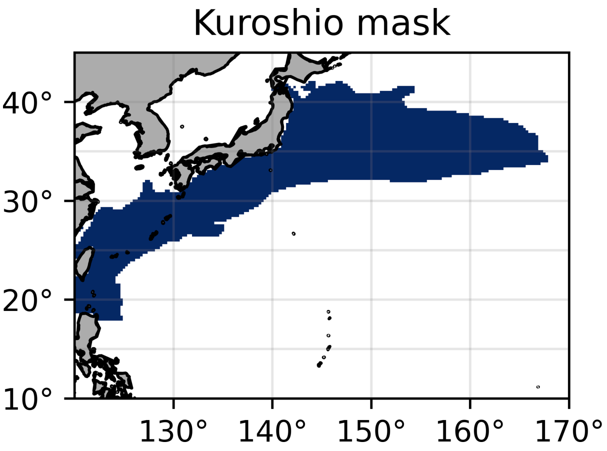

FIG. A3. The Kuroshio mask is defined as grid where the KE exceeds than 5 J m^{-3}.

REFERENCES

An, B., and Coauthors, 2023: The benefits of high-resolution models in simulating the Kuroshio extension and its long-term changes. *Climate Dyn.*, **61**, 5407–5427, https://doi.org/10.1007/s00382-023-06862-z.

Chang, M.-H., S. Jan, V. Mensah, M. Andres, L. Rainville, Y. J. Yang, and Y.-H. Cheng, 2018: Zonal migration and transport variations of the Kuroshio East of Taiwan induced by eddy impingements. *Deep-Sea Res. I*, **131**, 1–15, https://doi.org/10.1016/j.dsr.2017.11.006.

Chen, C., G. Wang, S.-P. Xie, and W. Liu, 2019: Why does global warming weaken the Gulf Stream but intensify the Kuroshio? *J. Climate*, **32**, 7437–7451, https://doi.org/10.1175/JCLI-D-18-0895.1.

Cheon, W. G., Y.-G. Park, S.-W. Yeh, and B.-M. Kim, 2012: Atmospheric impact on the northwestern Pacific under a global warming scenario. *Geophys. Res. Lett.*, **39**, L16709, https://doi.org/10.1029/2012GL052364.

Choi, B.-H., D.-H. Kim, and J.-W. Kim, 2002: Regional responses of climate in the northwestern Pacific Ocean to gradual global warming for a CO_2 quadrupling. *J. Meteor. Soc. Japan*, **80**, 1427–1442, https://doi.org/10.2151/jmsj.80.1427.

Chow, C. H., Y.-H. Tseng, H.-H. Hsu, and C.-C. Young, 2017: Interannual variability of the subtropical countercurrent eddies in the North Pacific associated with the western-Pacific teleconnection pattern. *Cont. Shelf Res.*, **143**, 175–184, https://doi.org/10.1016/j.csr.2016.08.006.

Davis, N. A., and T. Birner, 2022: Eddy-mediated Hadley cell expansion due to axisymmetric angular momentum adjustment to greenhouse gas forcings. *J. Atmos. Sci.*, **79**, 141–159, https://doi.org/10.1175/JAS-D-20-0149.1.

Delworth, T. L., and Coauthors, 2012: Simulated climate and climate change in the GFDL CM2.5 high-resolution coupled climate model. *J. Climate*, **25**, 2755–2781, https://doi.org/10.1175/JCLI-D-11-00316.1.

Douglass, E. M., Y.-O. Kwon, and S. R. Jayne, 2013: A comparison of North Pacific and North Atlantic subtropical mode waters in a climatologically-forced model. *Deep-Sea Res. II*, **91**, 139–151, https://doi.org/10.1016/j.dsr2.2013.02.023.

Gent, P. R., and J. C. Mcwilliams, 1990: Isopycnal mixing in ocean circulation models. *J. Phys. Oceanogr.*, **20**, 150–155, https://doi.org/10.1175/1520-0485(1990)020<0150:IMIOCM>2.0.CO;2.

Hallberg, R., 2013: Using a resolution function to regulate parameterizations of oceanic mesoscale eddy effects. *Ocean Modell.*, **72**, 92–103, https://doi.org/10.1016/j.ocemod.2013.08.007.

Hanawa, K., and L. D. Talley, 2001: Mode waters. *Ocean Circulation and Climate*, G. Siedler, J. Church, and J. Gould, Eds., International Geophysics Series, Vol. 77, Elsevier, 373–386.

Hu, S., J. Sprintall, C. Guan, M. J. McPhaden, F. Wang, D. Hu, and W. Cai, 2020: Deep-reaching acceleration of global mean ocean circulation over the past two decades. *Sci. Adv.*, **6**, eaax7727, https://doi.org/10.1126/sciadv.aax7727.

Hunke, E., W. Lipscomb, P. Jones, A. Turner, N. Jeffery, and S. Elliott, 2017: CICE, The Los Alamos Sea Ice Model. USDOE, https://www.osti.gov//servlets/purl/1364126.

Hurlburt, H. E., A. J. Wallcraft, W. J. Schmitz Jr., P. J. Hogan, and E. J. Metzger, 1996: Dynamics of the Kuroshio/Oyashio current system using eddy-resolving models of the North Pacific Ocean. *J. Geophys. Res.*, **101**, 941–976, https://doi.org/10.1029/95JC01674.

Jayne, S. R., N. G. Hogg, and P. Malanotte-Rizzoli, 1996: Recirculation gyres forced by a beta-plane jet. *J. Phys. Oceanogr.*, **26**, 492–504, https://doi.org/10.1175/1520-0485(1996)026<0492:RGFBAB>2.0.CO;2.

Kida, S., and Coauthors, 2016: Oceanic fronts and jets around Japan: A review. *"Hot Spots" in the Climate System: New Developments in the Extratropical Ocean-Atmosphere Interaction Research*, H. Nakamura et al., Eds., Springer, 1–30, https://doi.org/10.1007/978-4-431-56053-1_1.

Kirtman, B. P., and Coauthors, 2012: Impact of ocean model resolution on CCSM climate simulations. *Climate Dyn.*, **39**, 1303–1328, https://doi.org/10.1007/s00382-012-1500-3.

Large, W. G., and S. G. Yeager, 2009: The global climatology of an interannually varying air–sea flux data set. *Climate Dyn.*, **33**, 341–364, https://doi.org/10.1007/s00382-008-0441-3.

——, J. C. McWilliams, and S. C. Doney, 1994: Oceanic vertical mixing: A review and a model with a nonlocal boundary layer parameterization. *Rev. Geophys.*, **32**, 363–403, https://doi.org/10.1029/94RG01872.

Lin, P., J. Ma, F. Chai, P. Xiu, and H. Liu, 2020: Decadal variability of nutrients and biomass in the southern region of Kuroshio extension. *Prog. Oceanogr.*, **188**, 102441, https://doi.org/10.1016/j.pocean.2020.102441.

Lu, J., G. A. Vecchi, and T. Reichler, 2007: Expansion of the Hadley cell under global warming. *Geophys. Res. Lett.*, **34**, L06805, https://doi.org/10.1029/2006GL028443.

Ma, X., and Coauthors, 2016: Western boundary currents regulated by interaction between ocean eddies and the atmosphere. *Nature*, **535**, 533–537, https://doi.org/10.1038/nature18640.

Marshall, J., and G. Nurser, 1986: Steady, free circulation in a stratified quasi-geostrophic ocean. *J. Phys. Oceanogr.*, **16**, 1799–1813, https://doi.org/10.1175/1520-0485(1986)016<1799:SFCIAS>2.0.CO;2.

Martínez-Moreno, J., A. M. Hogg, M. H. England, N. C. Constantinou, A. E. Kiss, and A. K. Morrison, 2021: Global changes in oceanic mesoscale currents over the satellite altimetry record. *Nat. Climate Change*, **11**, 397–403, https://doi.org/10.1038/s41558-021-01006-9.

Peng, Q., S.-P. Xie, D. Wang, R. X. Huang, G. Chen, Y. Shu, J.-R. Shi, and W. Liu, 2022: Surface warming–induced global acceleration of upper ocean currents. *Sci. Adv.*, **8**, eabj8394, https://doi.org/10.1126/sciadv.abj8394.

Qiu, B., and S. Chen, 2005: Variability of the Kuroshio extension jet, recirculation gyre, and mesoscale eddies on decadal time scales. *J. Phys. Oceanogr.*, **35**, 2090–2103, https://doi.org/10.1175/JPO2807.1.

——, and ——, 2010: Eddy-mean flow interaction in the decadally modulating Kuroshio Extension system. *Deep-Sea Res. II*, **57**, 1098–1110, https://doi.org/10.1016/j.dsr2.2008.11.036.

——, ——, L. Wu, and S. Kida, 2015: Wind-versus eddy-forced regional sea level trends and variability in the North Pacific Ocean. *J. Climate*, **28**, 1561–1577, https://doi.org/10.1175/JCLI-D-14-00479.1.

Sakamoto, T. T., H. Hasumi, M. Ishii, S. Emori, T. Suzuki, T. Nishimura, and A. Sumi, 2005: Responses of the Kuroshio and the Kuroshio extension to global warming in a high-resolution climate model. *Geophys. Res. Lett.*, **32**, L14617, https://doi.org/10.1029/2005GL023384.

Sasaki, Y. N., and C. Umeda, 2021: Rapid warming of sea surface temperature along the Kuroshio and the China coast in the East China Sea during the twentieth century. *J. Climate*, **34**, 4803–4815, https://doi.org/10.1175/JCLI-D-20-0421.1.

Sato, Y., S. Yukimoto, H. Tsujino, H. Ishizaki, and A. Noda, 2006: Response of North Pacific Ocean circulation in a

Kuroshio-resolving ocean model to an Arctic Oscillation (AO)-like change in Northern Hemisphere atmospheric circulation due to greenhouse-gas forcing. *J. Meteor. Soc. Japan*, **84**, 295–309, https://doi.org/10.2151/jmsj.84.295.

Seager, R., Y. Kushnir, N. H. Naik, M. A. Cane, and J. Miller, 2001: Wind-driven shifts in the latitude of the Kuroshio–Oyashio extension and generation of SST anomalies on decadal timescales. *J. Climate*, **14**, 4249–4265, https://doi.org/10.1175/1520-0442(2001)014<4249:WDSITL>2.0.CO;2.

Sen Gupta, A., A. Ganachaud, S. McGregor, J. N. Brown, and L. Muir, 2012: Drivers of the projected changes to the Pacific Ocean equatorial circulation. *Geophys. Res. Lett.*, **39**, L09605, https://doi.org/10.1029/2012GL051447.

——, S. McGregor, E. van Sebille, A. Ganachaud, J. N. Brown, and A. Santoso, 2016: Future changes to the Indonesian throughflow and Pacific circulation: The differing role of wind and deep circulation changes. *Geophys. Res. Lett.*, **43**, 1669–1678, https://doi.org/10.1002/2016GL067757.

——, A. Stellema, G. M. Pontes, A. S. Taschetto, A. Vergés, and V. Rossi, 2021: Future changes to the upper ocean western boundary currents across two generations of climate models. *Sci. Rep.*, **11**, 9538, https://doi.org/10.1038/s41598-021-88934-w.

Small, R. J., and Coauthors, 2008: Air–sea interaction over ocean fronts and eddies. *Dyn. Atmos. Oceans*, **45**, 274–319, https://doi.org/10.1016/j.dynatmoce.2008.01.001.

Tseng, Y.-H., M.-L. Shen, S. Jan, D. E. Dietrich, and C.-P. Chiang, 2012: Validation of the Kuroshio Current system in the dual-domain Pacific Ocean model framework. *Prog. Oceanogr.*, **105**, 102–124, https://doi.org/10.1016/j.pocean.2012.04.003.

——, and Coauthors, 2016: North and equatorial Pacific Ocean circulation in the CORE-II hindcast simulations. *Ocean Modell.*, **104**, 143–170, https://doi.org/10.1016/j.ocemod.2016.06.003.

——, S.-E. Tsao, Y.-C. Kuo, and J.-Y. Tsai, 2022: TIMCOM model datasets for the CMIP6 Ocean Model Intercomparison Project. *Ocean Modell.*, **179**, 102109, https://doi.org/10.1016/j.ocemod.2022.102109.

Tsubouchi, T., T. Suga, and K. Hanawa, 2016: Comparison study of subtropical mode waters in the world ocean. *Front. Mar. Sci.*, **3**, 270, https://doi.org/10.3389/fmars.2016.00270.

Wang, L., Q. Liu, L. Xu, and S.-P. Xie, 2013: Response of mode water and subtropical countercurrent to greenhouse gas and aerosol forcing in the North Pacific. *J. Ocean Univ. China*, **12**, 222–229, https://doi.org/10.1007/s11802-013-2193-x.

Wang, Y.-L., C.-R. Wu, and S.-Y. Chao, 2016: Warming and weakening trends of the Kuroshio during 1993–2013. *Geophys. Res. Lett.*, **43**, 9200–9207, https://doi.org/10.1002/2016GL069432.

Waterman, S., and S. R. Jayne, 2011: Eddy-mean flow interactions in the along-stream development of a western boundary current jet: An idealized model study. *J. Phys. Oceanogr.*, **41**, 682–707, https://doi.org/10.1175/2010JPO4477.1.

Weijer, W., W. Cheng, O. A. Garuba, A. Hu, and B. T. Nadiga, 2020: CMIP6 models predict significant 21st century decline of the Atlantic meridional overturning circulation. *Geophys. Res. Lett.*, **47**, e2019GL086075, https://doi.org/10.1029/2019GL086075.

Williams, P. D., 2009: A proposed modification to the Robert–Asselin time filter. *Mon. Wea. Rev.*, **137**, 2538–2546, https://doi.org/10.1175/2009MWR2724.1.

Wu, B., X. Lin, and L. Yu, 2021: Poleward shift of the Kuroshio extension front and its impact on the North Pacific subtropical mode water in the recent decades. *J. Phys. Oceanogr.*, **51**, 457–474, https://doi.org/10.1175/JPO-D-20-0088.1.

Wu, L., and Coauthors, 2012: Enhanced warming over the global subtropical western boundary currents. *Nat. Climate Change*, **2**, 161–166, https://doi.org/10.1038/nclimate1353.

Xie, S.-P., L. Xu, Q. Liu, and F. Kobashi, 2011: Dynamical role of mode water ventilation in decadal variability in the central subtropical gyre of the North Pacific. *J. Climate*, **24**, 1212–1225, https://doi.org/10.1175/2010JCLI3896.1.

Yamanaka, G., and Coauthors, 2021: Projected climate change in the western North Pacific at the end of the 21st century from ensemble simulations with a high-resolution regional ocean model. *J. Oceanogr.*, **77**, 539–560, https://doi.org/10.1007/s10872-021-00593-7.

Yang, H., G. Lohmann, W. Wei, M. Dima, M. Ionita, and J. Liu, 2016: Intensification and poleward shift of subtropical western boundary currents in a warming climate. *J. Geophys. Res. Oceans*, **121**, 4928–4945, https://doi.org/10.1002/2015JC011513.

Young, C.-C., Y.-C. Liang, Y.-H. Tseng, and C.-H. Chow, 2014: Characteristics of the raw-filtered leapfrog time-stepping scheme in the ocean general circulation model. *Mon. Wea. Rev.*, **142**, 434–447, https://doi.org/10.1175/MWR-D-12-00333.1.

Zhang, X., Q. Wang, and M. Mu, 2017: The impact of global warming on Kuroshio extension and its southern recirculation using CMIP5 experiments with a high-resolution climate model MIROC4h. *Theor. Appl. Climatol.*, **127**, 815–827, https://doi.org/10.1007/s00704-015-1672-y.